



Research Article

Mechanism of subsurface microstructural fatigue crack initiation during high and very-high cycle fatigue of advanced bainitic steels

Guhui Gao^{a,*}, Rong Liu^a, Yusong Fan^a, Guian Qian^b, Xiaolu Gui^a, R.D.K. Misra^c, Bingzhe Bai^{a,d}

^a Material Science & Engineering Research Center, School of Mechanical, Electronic and Control Engineering, Beijing Jiaotong University, Beijing 100044, China

^b State Key Laboratory of Nonlinear Mechanics (LNM), Institute of Mechanics, Chinese Academy of Sciences, Beijing 100190, China

^c Laboratory for Excellence in Advanced Steel Research, Department of Metallurgical, Materials and Biomedical Engineering, University of Texas at El Paso, 500W University Avenue, El Paso, TX 79968, USA

^d Key Laboratory of Advanced Material, School of Material Science and Engineering, Tsinghua University, Beijing 100084, China



ARTICLE INFO

Article history:

Received 6 March 2021

Revised 6 July 2021

Accepted 2 August 2021

Available online 28 October 2021

Keywords:

Microstructure

Advanced bainitic steels

Very high cycle fatigue

Mechanism

Retained austenite

ABSTRACT

Advanced bainitic steels with the multiphase structure of bainitic ferrite, retained austenite and martensite exhibit distinctive fatigue crack initiation behavior during high cycle fatigue/very high cycle fatigue (HCF/VHCF) regimes. The subsurface microstructural fatigue crack initiation, referred to as “non-inclusion induced crack initiation, NIICI”, is a leading mode of failure of bainitic steels within the HCF/VHCF regimes. In this regard, there is currently a missing gap in the knowledge with respect to the cyclic response of multiphase structure during VHCF failure and the underlying mechanisms of fatigue crack initiation during VHCF. To address this aspect, we have developed a novel approach that explicitly identifies the knowledge gap through an examination of subsurface crack initiation and interaction with the local microstructure. This was accomplished by uniquely combining electron microscopy, three-dimensional confocal microscopy, focused ion beam, and transmission Kikuchi diffraction. Interestingly, the study indicated that there are multiple micro-mechanisms responsible for the NIICI failure of bainitic steels, including two scenarios of transgranular-crack-assisted NIICI and two scenarios of intergranular-crack-assisted NIICI, which resulted in the different distribution of fine grains in the crack initiation area. The fine grains were formed through fragmentation of bainitic ferrite lath caused by localized plastic deformation or via local continuous dynamic recrystallization because of repeated interaction between slip bands and prior austenite grain boundaries. The formation of fine grains assisted the advancement of small cracks. Another important aspect discussed is the role of retained austenite (RA) during cyclic loading, on crack initiation and propagation in terms of the morphology, distribution and stability of RA, which determined the development of localized cyclic plastic deformation in multiphase structure.

© 2022 Published by Elsevier Ltd on behalf of The editorial office of Journal of Materials Science & Technology.

1. Introduction

Advanced carbide-free bainitic (CFB) steels have recently attracted increased attention in view of their excellent combination of strength, ductility and toughness in the last decades [1–3]. By alloying steel with silicon and/or aluminum, the precipitation of cementite during bainitic transformation can be suppressed [2,3]. The carbon that is rejected from bainitic ferrite enriches the austenite during bainitic transformation, thereby promoting the

formation of retained austenite (RA) at ambient temperature. The potential applications of advanced bainitic steels are in the transportation industries, such as railway switch, train wheel, axle and bearing [4,5]. In order to improve the efficiency of transportation and save resources, many efforts are being made to have a higher strength/weight ratio of structural components, as well as higher traveling speed combined with a very long service life [6,7]. For instance, the high strength bainitic wheels used in the high-speed train are required to endure up to 10^8 loading cycles within one maintenance period [6]. However, the current design of railway components against fatigue failure is based on fatigue limit data in the high cycle fatigue (HCF) regime around 10^7 cycles, or only 5×10^6 cycles. Despite the cyclic stress below the traditional

* Corresponding author.

E-mail address: gaogh@bjtu.edu.cn (G. Gao).

fatigue limit, fatigue failure continues to occur beyond 10^7 cycles [8–10]. In this context, very high cycle fatigue (VHCF, *i.e.*, enduring cyclic stress in excess of 10^7 cycles) behavior of bainitic steels is an important and challenging subject to ensure the long-term safety of structural components.

In general, there is a transition of fatigue crack initiation sites from specimen surface to subsurface inclusions or pores when the fatigue failure takes place within the VHCF regimes [8–10]. Numerous studies revealed that the non-metallic inclusions have a determining role in the VHCF properties of high strength steels [8–11]. In most cases, the subsurface inclusions acting as nucleation sites are usually surrounded by an “initiation characteristic area” inside the “fish-eye”. This initiation characteristic area (ICA) was designated as “optically dark area, ODA” [12], “granular bright facet, GBF” [13], or “fine granular area, FGA” [14]. It is reported that the formation of ICA consumes more than 95% of total life [15]. Thus, investigation on the ICA is very important to understand the failure mechanisms of VHCF [12–15]. Recently, microstructural characterization studies showed that there is a three-dimensional fine grains layer beneath the ICA in the vicinity of inclusions [14,16–21]. The role of the fine grains layer in the VHCF failure has attracted significant scientific interest but remains controversial and unclear [21]. On one hand, it is considered that the local grain refinement during VHCF occurs because of the repeated contact of the fracture surface along the crack wake, thus the formation of the fine grains layer is a consequence of VHCF failure. For instance, the “numerous cyclic pressing, NCP” model proposed by Hong et al. [17] supported this view. On the other hand, it is suggested that the grain refinement is a consequence of dislocation rearrangement and the formation of fine grains reduces the local threshold for the propagation of crack and enables the advancement of small cracks. Thus, the formation of fine grains layer is a prerequisite for crack initiation and is responsible for VHCF failure. The models such as “local grain refinement at crack tip” [16] and “fragmentation of martensitic laths and formation of dislocation cells” [20] agree with the latter view.

Besides the subsurface inclusion-induced crack initiation, the microstructure also affects the VHCF behavior of metallic materials [22], where fatigue crack initiates directly from the subsurface microstructure rather than from the inclusion [23–25]. We refer to crack initiation from subsurface microstructure as “non-inclusion-induced crack initiation, NIICI”, to distinguish it from “inclusion induced crack initiation, IICI” [26]. The NIICI phenomenon was observed in high strength steels and Ti or Ni alloys [27–29]. Our previous works analyzed the effect of microstructure and inclusion size on the VHCF behavior of bainite/martensite multiphase steels and revealed that there is competition between NIICI failure and IICI failure [26]. NIICI is one of the most important fatigue failure modes in VHCF regime for the bainitic steels [24–26]. It is suggested that the coarse bainite or blocky RA is responsible for the crack initiation, but the mechanism of damage continues to be unclear [26]. Similar to the fracture surface of IICI, the ICA within the “fish-eye” is also formed in the NIICI fracture surface [25,26]. However, it is uncertain whether the fine grains layer observed in ICA of IICI fracture surface is formed in ICA for NIICI failure to occur. Murakami et al. observed that the fine granular area (rough area) was only observed in the case of crack initiation around the inclusions but not for the bainitic area induced crack initiation, and thus proposed “hydrogen-assisted crack growth” [12]. But Pan and Hong reported the existence of a rough area for the NIICI fracture surface of Ti alloys [27]. In addition, the three-dimensional observations indicated that ICA for NIICI failure is actually composed of a micro-facet and a surrounding wavy area [30]. The micro-facet is close to the plane of maximum shear stress and is essentially

resulted from the fracture surface of the stage-I small crack, and the surrounding wavy area corresponds to the transition area from stage-I small crack to stage-II long crack. In general, the stage-I crack has a length comparable with the grain dimension and is very sensitive to the microstructure. The stage-I crack grows along with the preferred orientated slip system with maximum resolved shear stress. The stage-II crack is less sensitive to the microstructure and is aligned perpendicular to the maximum tensile direction [31]. Similarly, Chai [32] also considered that the crack propagation inside ICA of subsurface non-defect fatigue crack origins is stage-I cracking influenced by the microstructure. A recent work by Abdesselam et al. [33] assumed that the early growth of crack occurs very slowly similar to stage-I like crack propagation, thus proposed the model of “stage-I like crack propagation with grain refinement in the crack wakes”. In this case, the local microstructural evolution during VHCF and the interaction with small cracks determined the process of fatigue crack initiation.

The effect of microstructure and stress/strain amplitude on low-cycle fatigue (LCF) and HCF behavior of bainitic steels has been analyzed [34–37]. For example, the recent works on LCF behavior of bainitic steel by Marinelli et al. [37] revealed that the strain amplitude ($\Delta\varepsilon_p$) affects the cracking mechanisms, *e.g.*, the micro-cracks nucleated either in bainitic ferrite lath with highest Schmid factor or at high-angle bainitic block boundaries, depending on $\Delta\varepsilon_p$ [37]. However, the mechanism of microstructure-induced small crack initiation of CFB steels during VHCF with much lower stress/strain amplitude was still not fully understood. For example, it is unclear how small cracks overcome the microstructural barriers of bainitic ferrite lath or block boundaries and whether it accompanies the formation of fine grains layer.

In addition, there is an increasing interest in steels containing large content of RA, while there is a consensus that RA improves mechanical properties related to monotonic loading, such as elongation and toughness [1]. But the effect of RA in bainite microstructure on fatigue crack initiation is relatively complex. On the one hand, compared with bainitic ferrite and martensite, the austenite is a soft phase, which is prone to localized plastic deformation and induces fatigue crack initiation because of local plasticity exhaustion or generation of high stress concentrations at the phase boundaries [38,39]. On the other hand, the metastable austenite in the fatigue crack tip zone can transform to martensite because of local plastic deformation, which decelerates the fatigue crack growth via absorbed energy and crack closure effects [40,41]. A recent investigation on ferrite/austenite duplex steels by Fu et al. [42] showed that the austenite phase exhibits cyclic softening-hardening-softening behavior in the VHCF regime, which affects load stress partitioning and formation of micro-cracks. The RA in bainite exhibits different morphologies with different distribution, carbon enrichment and mechanical stability. Our recent study revealed these microstructure features of RA significantly affect the formation and early growth of small cracks [30,43]. Hence, the understanding of the role of RA in crack initiation during VHCF requires an in-depth understanding.

In the present work, HCF/VHCF tests of CFB steels with two levels of size of inclusion were carried out, with the aim to unravel the mechanisms associated with subsurface microstructural fatigue cracking of bainitic steel. To address this aspect, we have developed a novel approach that explicitly identifies the knowledge gap through an examination of subsurface crack initiation and interaction with the local microstructure. This was accomplished by uniquely combining electron microscopy, 3-dimensional confocal microscopy, focused ion beam (FIB), and transmission Kikuchi diffraction (TKD). The formation mechanism of the fine grains layer and the role of RA in crack initiation were discussed in detail.

2. Experimental procedure

2.1. Materials

The chemical composition of experimental steel was Fe-0.42C-2.2Mn-1.75Si-0.5Cr (wt%). Two types of melting processes were adopted: (i) melting in vacuum induction furnace and (ii) an additional electroslag remelting after conventional a vacuum melting, with the aim to reduce the size of non-metallic inclusions in the steels. Based on our previous work [26], the maximum inclusion size in steel was $\sim 98 \mu\text{m}$ after convention vacuum melting and $\sim 15 \mu\text{m}$ after electroslag remelting, respectively. The ingots were forged to 16 mm thickness after 1200 °C for 4 h. The forged plate was subsequently annealed at 900 °C, followed by furnace cooling. The as-received microstructure of forged plates was ferrite plus pearlite. Then the specimens cut from forged plates were austenitized at 880 °C for 45 min and bainitic austempered at 360 °C for 2 h (*i.e.*, BAT treatment is described in Ref. [44]). In brief, the BAT treatment involves an isothermal bainitic transformation at a temperature between bainitic start temperature (B_s) and martensitic start temperature (M_s). For convenience, the BAT steels without and with electroslag remelting are designated as U-BAT steel and E-BAT steel, respectively.

Microstructure before fatigue testing was characterized by scanning electron microscopy (SEM, Zeiss EVO18, 20 kV) and transmission electron microscopy (TEM, JEOL 2010, 200 kV). Electron backscatter diffraction (EBSD) measurement (step size: 0.1 μm) was carried out using Zeiss ULTRA-55 field emission SEM after electrolytic polishing. The electrolytic polishing was conducted at a voltage of 18 V and current of ~ 1 A in an electrolyte solution (8 vol.% perchloric acid, 10 vol.% distilled water, 10 vol.% 2-butoxyethanol and 72 vol.% ethanol). X-ray diffraction (XRD, Rigaku Smartlab, Cu K_α radiation) was used to determine the volume fraction of RA.

The undeformed BAT microstructure consists of bainitic ferrite (BF), film-like RA and blocky RA or martensite/austenite (M/A) islands, as shown in Fig. 1(a) and (b). The total volume fraction of RA is 0.22. The film-like RA with nanometer-size or submicron-size usually has higher carbon content and stacking fault energy than micrometer-sized blocky RA [43]. The bainitic ferrite exhibits a hierarchical structure with packet, block and lath. The bainitic ferrite lath consists of sub-lath and sub-units, which is associated with the transformation of bainite [45]. The inverse pole figure (IPF) map of bainitic ferrite and martensite (body-centered cubic structure) is shown in Fig. 1(c), where each color represents a single crystallographic variant (*i.e.* block). The corresponding pole figure (PF) of a single prior austenite grain reveals that there is Kurdjumov-Sachs (K-S) or Nishiyama-Wassermann (N-W) relationship between bainitic ferrite and parent austenite [46]. Microstructure characterization by SEM, TEM and EBSD indicates the width of bainitic ferrite lath is heterogeneous, and is in the range of 0.2–1.0 μm . The width of bainitic ferrite block is $3.2 \pm 1 \mu\text{m}$. It should be noted that the melting process has a negligible effect on the BAT microstructure after forging, annealing and heat treatment.

2.2. Fatigue test

The geometry and dimensions of the smooth round bar specimens for rotating bending fatigue testing were shown in Ref. [43]. After rough machining, the specimens were subjected to BAT heat treatment, followed by precision polishing before the fatigue test. The precision polishing process included machine grinding and final hand polishing with 2000# emery paper. Fatigue tests were conducted at different stress amplitudes at stress ratio $R = -1$ on PQ1-6 type rotating bending fatigue test machine (LETRY, PR

China). The loading frequency was ~ 83 Hz, and the tests were carried out at ambient atmosphere.

Crack initiation regions (*e.g.*, fish-eye and ICA area) of failure specimens were observed directly by SEM (ZEISS EVO 18, 20 kV) and 3-dimensional Confocal Microscope Phase Shift MicroXAM-3D (Vertical scan resolution: 0.01 μm , lateral resolution: 0.11 μm). Here, MicroXAM-3D could measure the surface profile of the fatigue fracture surface. Under the guidance of 3D topography, the FIB/SEM dual-beam system (Helios Nanolab 600i) was employed to cut the cross-sectional samples (thin foils with a thickness of ~ 100 nm) from fatigue crack initiation regions. Thin foils obtained by FIB/SEM dual-beam system were characterized by field emission TEM equipped with scanning TEM (STEM) facility (JEOL 2010F, 200 kV and FEI Tecnai F30, 300 kV), in order to observe the evolution of retained austenite and bainitic ferrite beneath the ICA area. TKD technology was also carried out on the thin foils using Oxford Nordlys Nano EBSD detector on ZEISS Merlin (at an acceleration voltage of 30 kV, with step size: 10–50 nm and tilt angle: 20°). Here, the angular resolution of TKD was $\sim 0.2^\circ$. The TKD data were post-processed by HKL CHANNEL 5 Flamenco and MTEX software [47]. The local misorientation distribution map was used to evaluate the localized plastic strain distribution among bainitic ferrite and RA. The local misorientation distribution component calculated the average misorientation between every pixel and its surrounding pixels, and assigned the mean value to that pixel. In the present study, 8 neighbors (*i.e.*, 3×3 arrays) were used in this calculation and the misorientation was not allowed to exceed 2° to exclude boundaries of laths. It is reported that the boundaries with misorientation exceed 2° often corresponded to lath boundaries [48].

3. Results

3.1. S-N characteristics

Fig. 2 shows S-N data obtained from the bending fatigue test of the E-BAT and U-BAT samples. As indicated in Fig. 2(a), the S-N data of failed specimens are approximated with a straight line in the double logarithmic diagram, and the relationship of fitting line is:

$$\log \sigma_a = 3.12 - 0.039 \log N_f \text{ with } R^2 = 0.87 \quad (1)$$

In addition, the E-BAT and U-BAT steels have similar S-N trend. It is worth noting that the fatigue failure eventually occurs with increase in the number of cycles even beyond 10^7 cycles, *i.e.* the infinite fatigue life cannot be obtained above 10^7 cycles, as shown in Fig. 2(a).

The symbols and abbreviations in Fig. 2(a) indicate the types of crack initiation mode and Fig. 2(b) shows the fraction of each mode of failed specimens. It can be seen that there are two crack initiation modes for the failed E-BAT samples: 27% of samples cracked on the surface and 73% of samples cracked by internal NI-ICI mode. The fatigue cracks initiate on the surface at relatively higher stress amplitude, which is related to the formation of extrusions and intrusions in surface grains because of the development of persistent slip bands [49]. When the stress amplitude decreases and N_f exceeds 10^6 cycles, the majority of fatigue cracks initiate from the sub-surface microstructure (*i.e.*, NIICI mode). Besides the surface-induced crack initiation and NIICI, the surface and subsurface inclusion-induced crack initiation modes are also observed in the failed U-BAT sample. Although the crack initiation modes of E-BAT and U-BAT steels are not entirely identical, the two experimental steels have similar S-N trend (Fig. 2(a)), which means that the microstructure has a significant effect on the fatigue properties of CFB steels in this study.

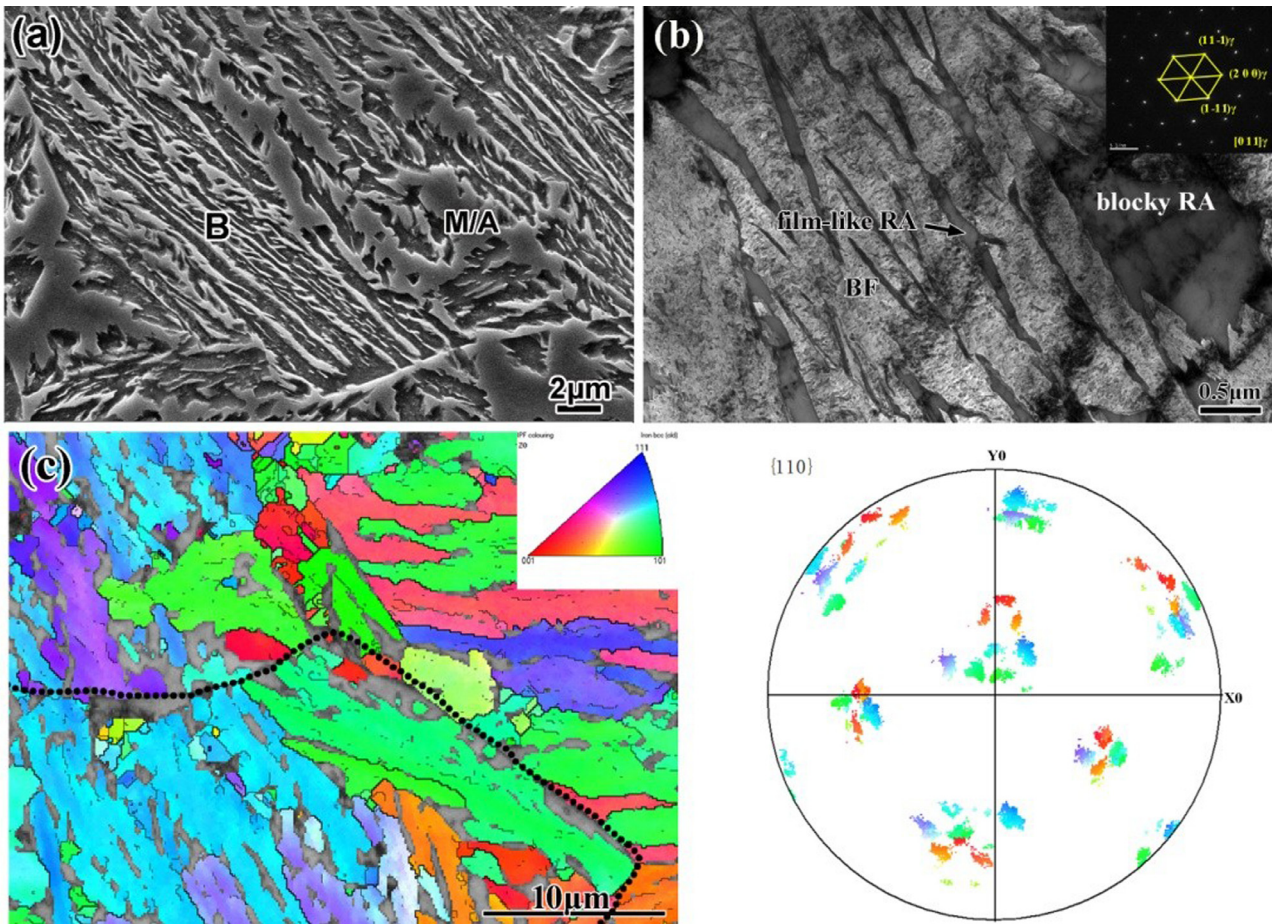


Fig. 1. Microstructures of BAT steels. (a) SEM micrograph; (b) TEM micrograph with electron diffraction pattern of RA [43]; (c) EBSD image combined with band contrast, inverse pole figure (IPF) and pole figure (PF) maps of bainitic ferrite and martensite, the dashed black line showing the boundary of a single prior austenite grain; B: bainite, M/A: martensite/austenite island, BF: bainitic ferrite, RA: retained austenite.

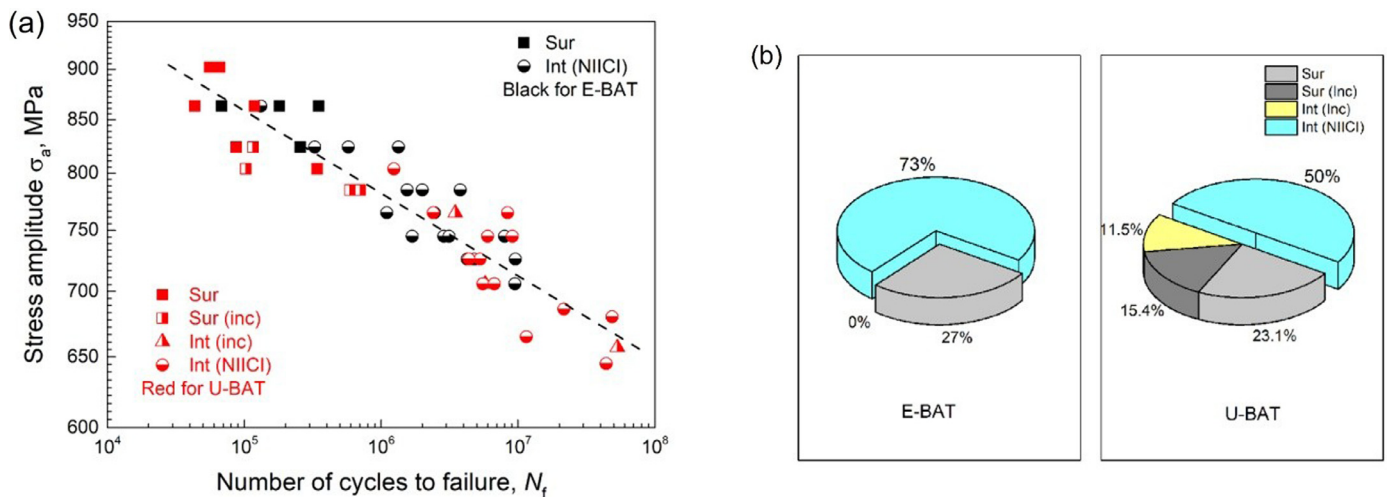


Fig. 2. (a) *S-N* data and (b) fraction of each fatigue crack initiation mode of failed E-BAT and U-BAT samples. Sur: surface, Sur (Inc): surface inclusion, Int (Inc): interior inclusion, Int (NIICI): interior non-inclusion induced crack initiation.

3.2. Geometrical morphology of fracture surface

Since the features of subsurface inclusion-induced fracture surface within HCF/VHCF regimes, such as fish-eye morphology, have been studied before [26,43], we discuss here the subsurface non-inclusion-induced fracture surface in detail. Figs. 3 and 4 show typical fracture surface of NIICI failed specimen within HCF and VHCF

regimes, respectively. The SEM images show that the fish-eye morphology with ICA is also formed in the NIICI fracture surfaces that are failed within both HCF and VHCF regimes. The ICA is rougher than the fish-eye area. Unlike the IICI fracture surface, no inclusion is observed in the center of ICA area, as indicated by the enlarged SEM images in Figs. 3(b) and 4(b). The 3D and surface profile observations (Figs. 3(c, d) and 4(c, d)) confirm that ICA in NIICI frac-

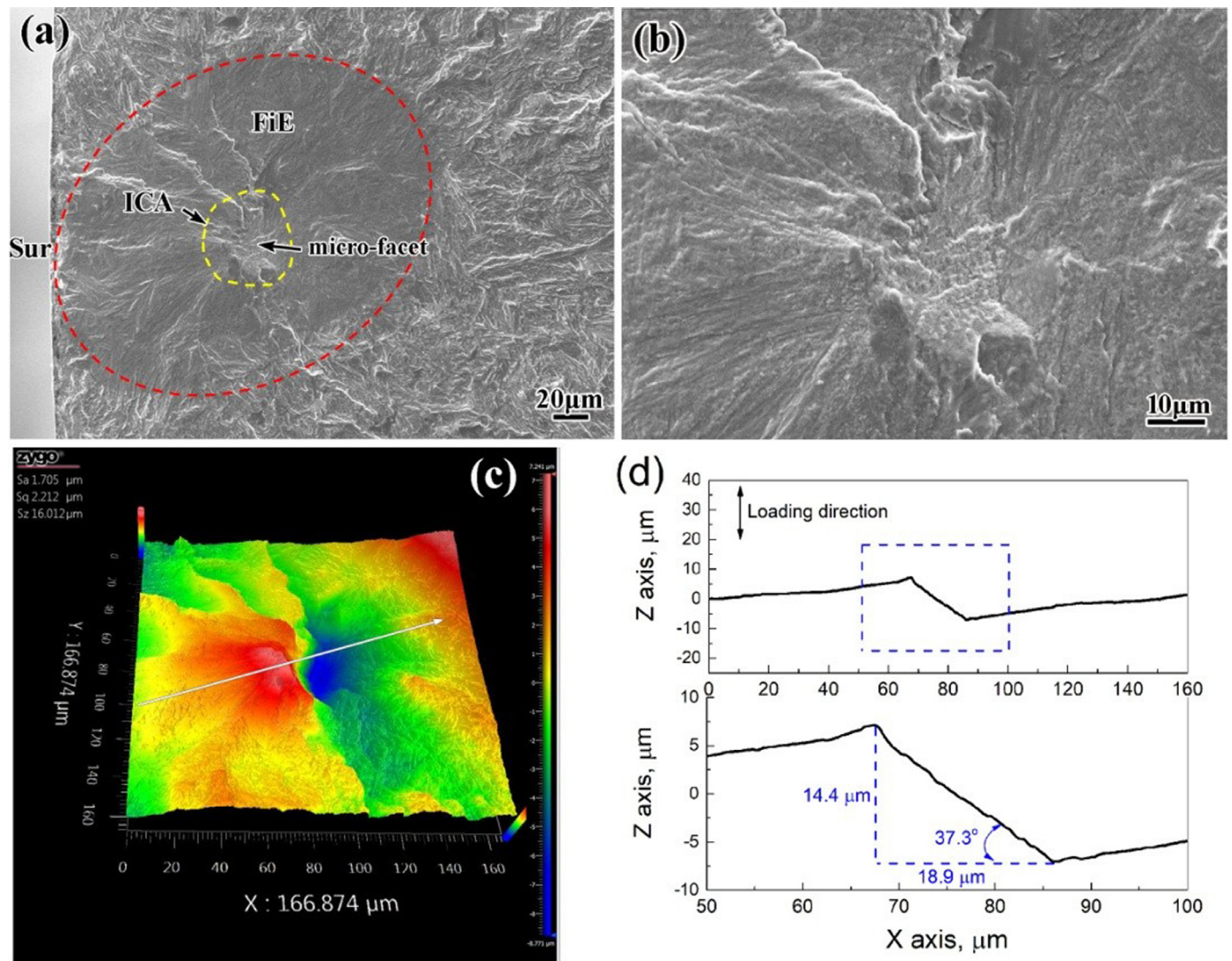


Fig. 3. (a) SEM image of a typical NIICI fracture surface of E-BAT specimen failed at $\sigma_a = 745$ MPa with $N_f = 1.69 \times 10^6$ cycles; (b) enlarged window of ICA area; (c) 3D morphology image; (d) the sectional profile of the labeled line in (c); Sur: surface, FiE: fish eye, ICA: initiation characteristic area.

ture surface is composed of a micro-facet and surrounding wavy area. There is an angle between 30° and 50° between the micro-facet and the plane of maximum tensile stress. The surface profile of micro-facet has a strong similarity with the propagation path of stage-I crack, which propagates on the special slip planes close to the plane of maximum shear stress [31]. The surrounding wavy area corresponds to the transition area (TA) from small microstructural crack to long crack, which is strongly related to the resistance offered by the microstructure [31,50]. The microstructural barrier affects the geometrical morphology of the transition area (TA), and also determines the periphery of ICA.

The values of stress intensity factor (SIF) range at the periphery of micro-facet (*i.e.*, ΔK_{fac}) and non-inclusion induced ICA (*i.e.*, ΔK_{NA}) in NIICI failed specimens and at the periphery of inclusion (*i.e.*, ΔK_{inc}) and ICA around inclusion (*i.e.*, ΔK_{IA}) in interior IICI failed specimens are calculated based on the $\sqrt{\pi \text{area}}$ model [51,52]:

$$\Delta K = 0.5\sigma_a (1 - d/R)\sqrt{\pi \text{area}} \quad (2)$$

where σ_a is stress amplitude, d is the depth of crack initiation site from surface of the failed specimen, R is the radius of the specimen, *area* is the projected area of inclusion, micro-facet and ICA on the plane perpendicular to the stress axis (the method of mea-

suring the projected area can be seen in Refs. [53,54] and the raw data can be seen in Supplementary materials). The calculated values of SIF versus the fatigue life are shown in Fig. 5. It is noted that the values of ΔK_{NA} lie within the same range as those of ΔK_{IA} , and are almost constant at an average value of $5.1 \text{ MPa m}^{1/2}$. Similarly, the values of ΔK_{fac} and ΔK_{inc} are also almost constant at an average value of $3.2 \text{ MPa m}^{1/2}$. The SIF of ICA (both ΔK_{NA} and ΔK_{IA}) is close to the threshold SIF for the propagation of long crack (*i.e.*, ΔK_{th} , $4.5 \text{ MPa m}^{1/2}$ for high strength steels [19]), whereas the SIF of micro-facet and inclusion (*i.e.*, ΔK_{fac} and ΔK_{inc}) is smaller than ΔK_{th} .

Based on 3D observation and SIF calculation of the characteristic area in NIICI fracture surface, it is suggested that the nucleation and early propagation of non-inclusion-induced cracks take place within the ICA area that contains a micro-facet and surrounding TA. The inclined angle of micro-facet, the size of micro-facet and ICA (or TA) are important geometrical parameters in controlling the initiation of non-inclusion induced cracks. In the following section, we describe in detail the characterization of microstructure beneath the micro-facet and TA in NIICI failed specimens, in order to fundamentally explore the relationship between the geometry and its surrounding microstructural evolution.

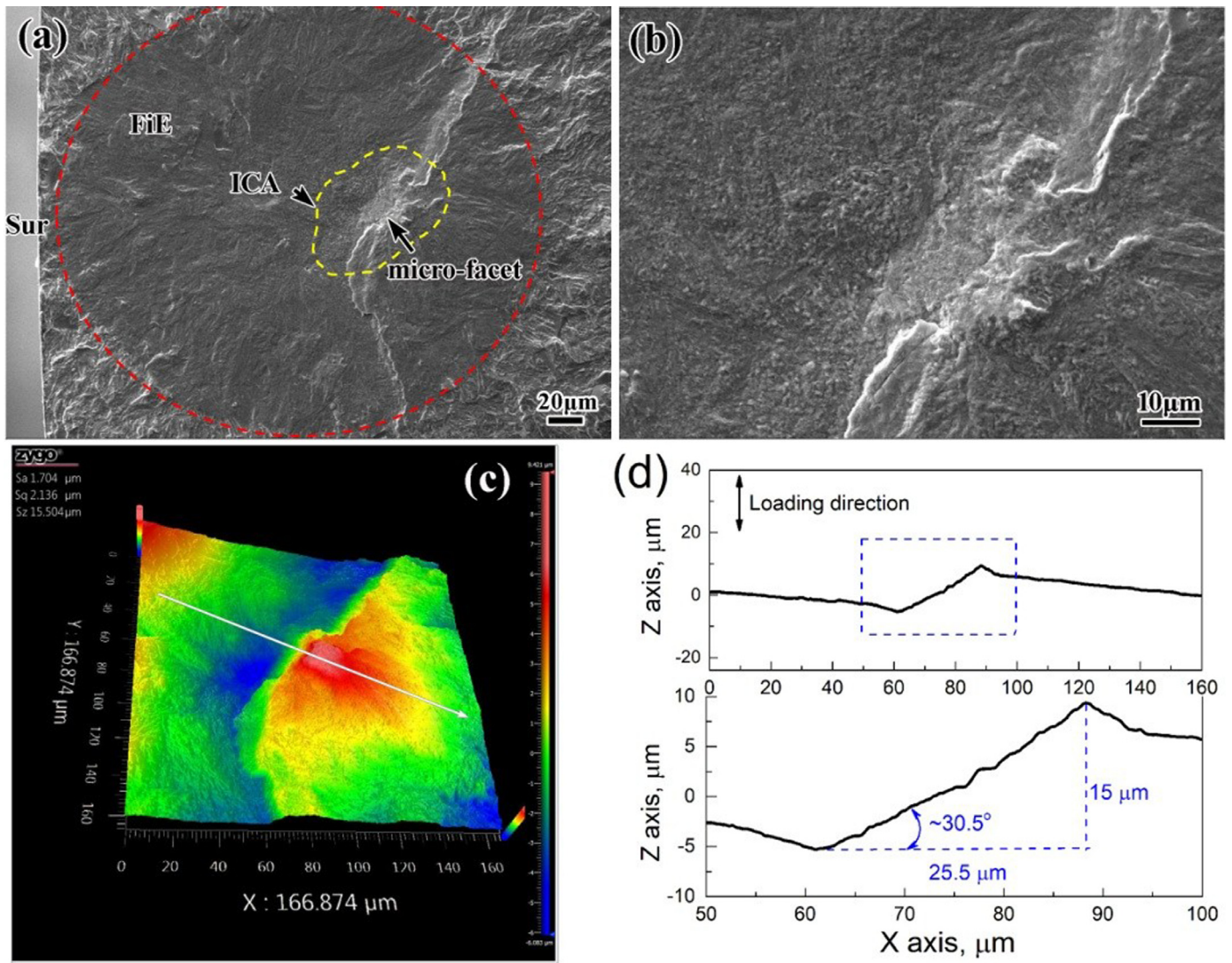


Fig. 4. (a) SEM image of a typical NIICI fracture surface of U-BAT specimen failed at $\sigma_a = 686$ MPa with $N_f = 2.16 \times 10^7$ cycles; (b) enlarged window of ICA area; (c) 3D morphology image; (d) the sectional profile of the labeled line in (c); Sur: surface, FiE: fish eye, ICA: initiation characteristic area.

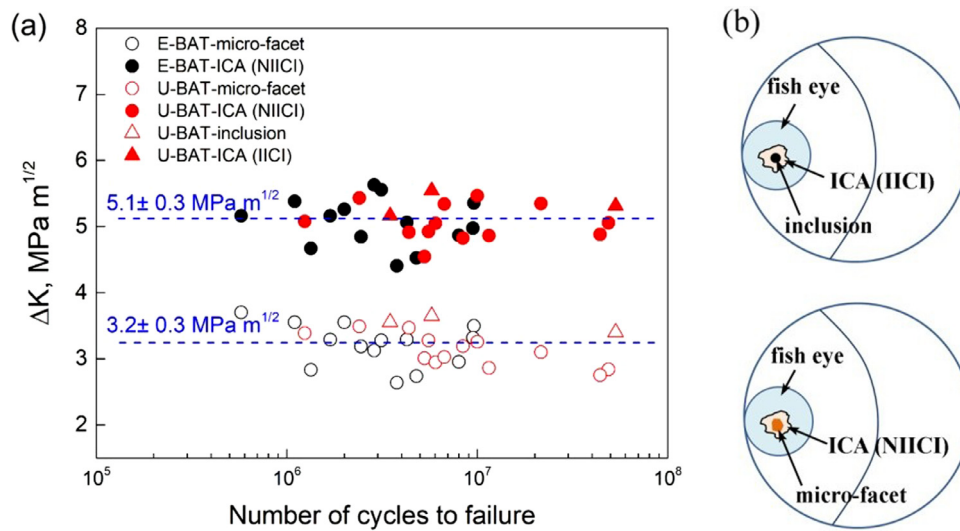


Fig. 5. (a) Stress intensity factor range of inclusions, micro-facet and ICA area of U-BAT and E-BAT specimens, the blue dash lines indicate the mean values; (b) Schematic showing the fish eye, ICA, facet and inclusion in the fracture surface (For interpretation of the references to color in this figure legend, the reader is referred to the web version of this article.).

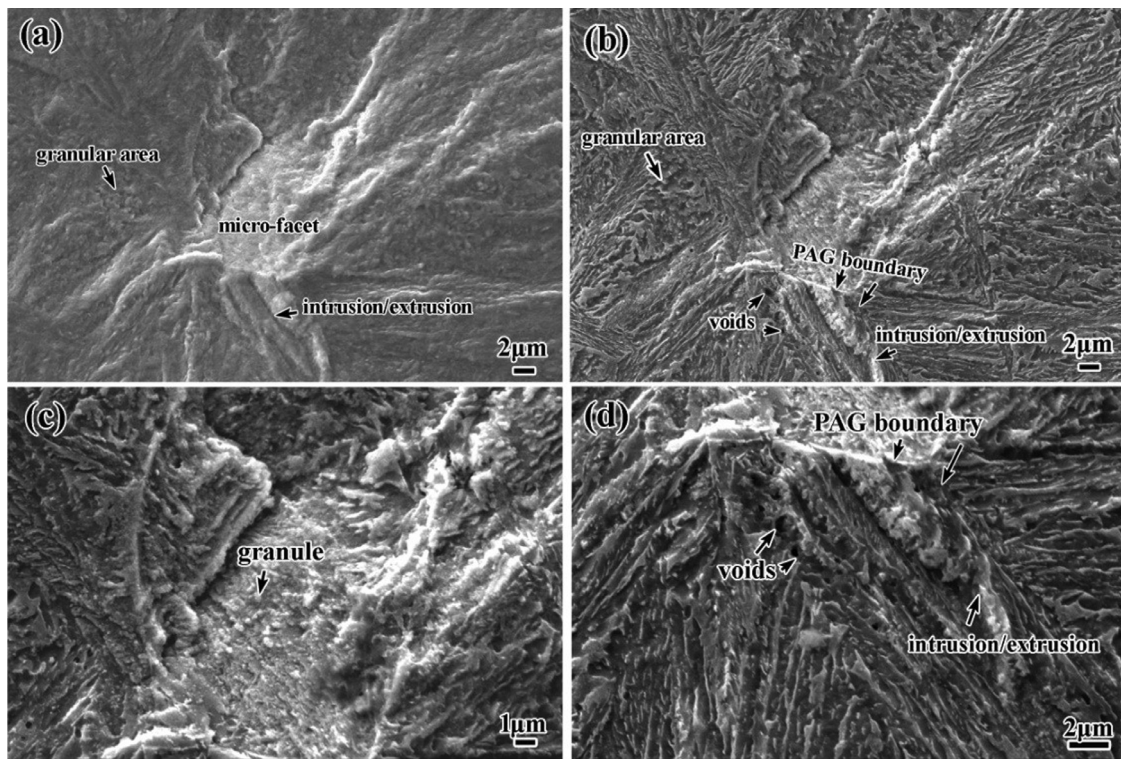


Fig. 6. SEM images of NIICI fracture surface (a) before and (b, c, d) after etching (E-BAT specimen failed at $\sigma_a = 785$ MPa with $N_f = 3.78 \times 10^6$ cycles), (c) and (d) are enlarged windows of (b). PAG: prior austenite grain.

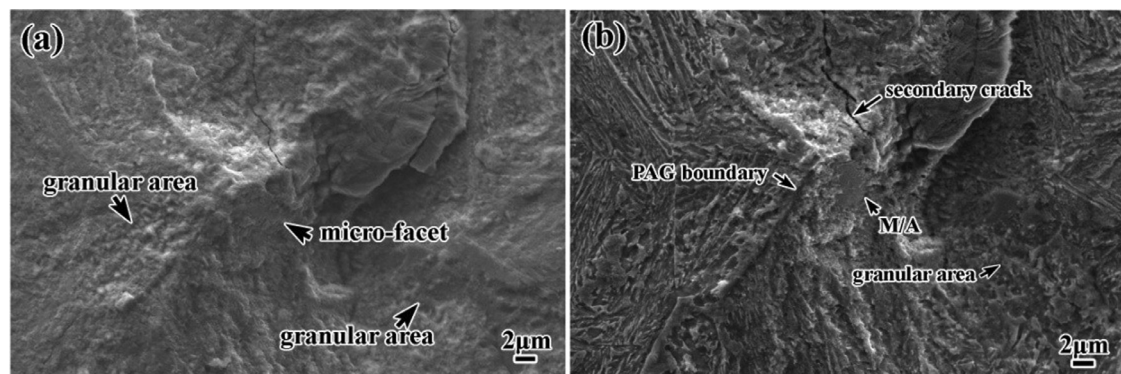


Fig. 7. SEM images of NIICI fracture surface. (a) before and (b) after etching (E-BAT specimen failed at $\sigma_a = 745$ MPa with $N_f = 7.99 \times 10^6$ cycles). PAG: prior austenite grain, M/A: martensite/austenite.

3.3. Etched fracture surface observation

In this section, several NIICI fracture surfaces with various stress amplitude and fatigue life are directly etched in a 2% nital solution, followed by SEM observation. Fig. 6 shows the NIICI fracture surface of the E-BAT sample failed at $\sigma_a = 785$ MPa with $N_f = 3.78 \times 10^6$ cycles. A comparison of fracture surfaces before and after etching reveals that the micro-facet is limited within a single prior austenite grain (PAG), as shown in Fig. 6(a) and (b). From the enlarged window of micro-facet in Fig. 6(c), the lath morphology is not very clear and there are several granules. The granular area and intrusion/extrusion are observed around the micro-facet, as shown by the unetched fracture surface in Fig. 6(a). After etching, the microstructure in the granular area shows fragmentation of bainitic ferrite laths (Fig. 6(b)). The voids within the bainitic ferrite lath are also observed from the etched fracture surface (Fig. 6(b) and (d)).

Fig. 7 shows the NIICI fracture surface of the E-BAT sample failed at $\sigma_a = 745$ MPa with $N_f = 7.99 \times 10^6$ cycles. It is observed that there is a blocky M/A constituent on the micro-facet, from the comparison of fracture surfaces before (Fig. 7(a)) and after etching (Fig. 7(b)). The blocky M/A is adjacent to the PAG boundary (Fig. 7(b)). Compared to bainitic ferrite, the etching of M/A is relatively feeble because of the presence of high carbon martensite and austenite [55]. Furthermore, the secondary cracks nucleate from M/A because of the brittle characteristic of M/A (Fig. 7(b)). The microstructure in the granular area around the micro-facet also shows fragmentation of bainitic ferrite laths (Fig. 7(b)).

Fig. 8 shows another NIICI fracture surface of the E-BAT sample failed at $\sigma_a = 706$ MPa with $N_f = 9.49 \times 10^6$ cycles. The comparison of fracture surfaces before and after etching reveals that the micro-facet is also limited within a single PAG, as shown in Fig. 8(a) and (b). A fraction of micro-facet is occupied by M/A (showing cleavage facet), while the other part exhibits fragmented

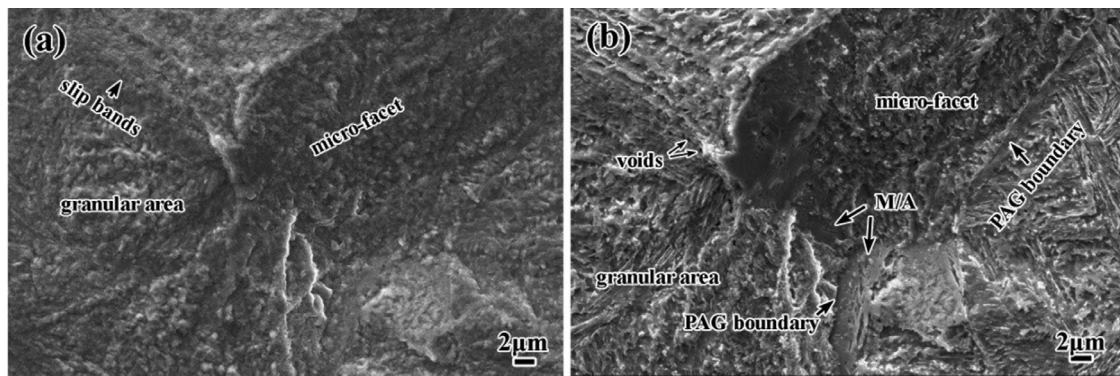


Fig. 8. SEM images of NIICI fracture surface. (a) Before and (b) after etching (E-BAT specimen failed at $\sigma_a = 706$ MPa with $N_f = 9.49 \times 10^6$ cycles).

microstructure (Fig. 8(b)). The presence of M/A in the neighboring PAG (Fig. 8(b)) is also observed. The granular area is also observed around the micro-facet. The slip bands are parallel to the longitudinal direction of bainitic ferrite lath. There are discontinuous voids formed within the bainitic ferrite laths along with slip bands. The granular area exhibits the character of fragmented microstructure.

3.4. Local microstructural evolution at crack initiation characteristic area

In this section, FIB is combined with TEM, STEM and TKD to acquire detailed information of high-resolution local microstructural evolution at crack initiation characteristic area (ICA). Fig. 9 shows microstructural characterization underneath the ICA in a typical NIICI fracture surface of the E-BAT specimen failed at $\sigma_a = 745$ MPa with $N_f = 2.87 \times 10^6$ cycles. Fig. 9(a) is the SEM image with a tilted angle showing the geometry of ICA and the position from where a thin foil sample is prepared using FIB. The thin foil sample covers a part of micro-facet and transition area (TA) and is characterized by TEM (Fig. 9(b)) and TKD (Fig. 9(c, d)). The micro-facet is inclined at about 40° to the loading axis, which implies that the micro-facet is close to the plane of maximum shear stress. TEM and TKD images confirm the presence of fine grains and voids along the micro-facet and TA. The IPF map in Fig. 9(c) combined with enlarged TEM images (Fig. 9(e, f)) reveals that the fine grains have the size between tens and hundreds of nanometers, and distribute along with a bainitic ferrite lath. Hence, the fine grains layer in micro-facet results from the fragmentation of bainitic ferrite laths [20]. There is also a tendency for the bainitic ferrite sub-block beneath micro-facet to fragment, as shown by a yellow ellipse in Fig. 9(c). The misorientation between sub-block I and II is less than 15° , hence the sub-blocks I and II are considered to make up a bainitic ferrite block [46]. The micro-facet is parallel to the longitudinal direction of the bainitic ferrite block. It is found that the activated slip planes of bainitic ferrite sub-blocks (I and II) aligned to the micro-facet have a high maximum Schmid factor ($SF = 0.406$ and 0.360 , respectively) rather than the highest maximum Schmid factor by means of slip trace analysis of $\{110\}_\alpha$ slip systems, as shown in Fig. 9(c). Based on the orientation relationship analysis, the bainitic ferrite sub-blocks (I and II) are adjacent to the PAG boundary. It is inferred that the fatigue failure is caused by intergranular cracking. The blocky RA on the other side of the PAG boundary is located between micro-facet and TA. The local misorientation map (Fig. 9(d)) indicates that RA has slightly higher local misorientation compared with bainitic ferrite, which implies that RA bears more local stress or plastic strain. The mean value of local misorientation of RA is about 0.54° , while that of bainitic ferrite is about 0.48° . TEM image and selected area diffraction patterns of RA in Fig. 9(g) show that the blocky RA does not transform

to martensite. In addition, there is a secondary crack that is normal to the longitudinal direction of bainitic ferrite lath. The fine grains are observed on the sides of secondary crack, but there is no fine grain at the front of the crack tip (Fig. 9(h)). The secondary crack does not continue to advance, possibly because of the barriers effect coming from lath/block boundaries [56].

Fig. 10 describes the microstructural characterization of the ICA in a typical NIICI fracture surface of the U-BAT specimen failed at $\sigma_a = 745$ MPa with $N_f = 9.09 \times 10^6$ cycles. Fig. 10(a) is the SEM image with a tilted angle showing the geometry of ICA and the position for preparation of the FIB sample. TEM image showing the overall microstructures underneath ICA is shown in Fig. 10(b). It is also found that the micro-facet is inclined at $\sim 45^\circ$ to the loading axis. There are several voids and secondary cracks underneath the ICA, which also distribute along the plane of maximum shear stress. Subsequently, the detailed characterizations were performed on two regions marked by the red dashed rectangle in Fig. 10(b).

The IPF and local misorientation maps of the region I are shown in Fig. 10(c and d), respectively. The presence of fine grains layer along the micro-facet and TA is noted. Enlarged TEM image of fine grains layer in Fig. 10(e) shows that the grain is more fine compared to the failed sample with shorter fatigue life in Fig. 9(e, f), which is confirmed by more complete selected area diffraction rings. The bainitic ferrite lath/block and inter-lath or inter-block RA are found beneath ICA. The micro-facet is aligned to the longitudinal direction of the bainitic ferrite block marked by α_1 , whose corresponding activated $\{110\}_\alpha$ slip plane also has a high maximum Schmid factor ($SF = 0.399$) rather than the highest maximum Schmid factor, as shown in Fig. 10(c). There are two RA grains with different orientations, as marked by $\gamma-1$ and $\gamma-2$, respectively, in Fig. 10(c). The thickness of $\gamma-1$ and $\gamma-2$ is ~ 250 nm (i.e., submicron-size). Based on the PTC Lab crystallography program [57], the orientation between $\gamma-1$ and $\gamma-2$ is calculated and is $[011] 67^\circ$, i.e., the two RA grains are twinned (e.g., the ideal orientation of twins is $[011] 60^\circ$). The orientation relationships (OR) between $\gamma-1$ and surrounding bainitic ferrite (marked by α_1 , α_2 and α_3) are listed in Table 1. It is found that $\gamma-1$ has a K-S relationship with both α_1 and α_3 , but the OR between $\gamma-1$ and α_2 deviates from the K-S relationship, as indicated in Table 1. It is implied that the α_2 lath or block experiences large plastic deformation, which can be confirmed by the local misorientation map in Fig. 10(d). The higher average angle of local misorientation is related to more plastic deformation [58]. Furthermore, the plastic deformation is concentrated near the fracture surface and in the regions between two RA grains ($\gamma-1$ and $\gamma-2$), as shown by the dashed line in Fig. 10(d). The local plastic deformation promotes the fragmentation of bainitic ferrite laths, and consequently the formation of voids, as shown in Fig. 10(f).

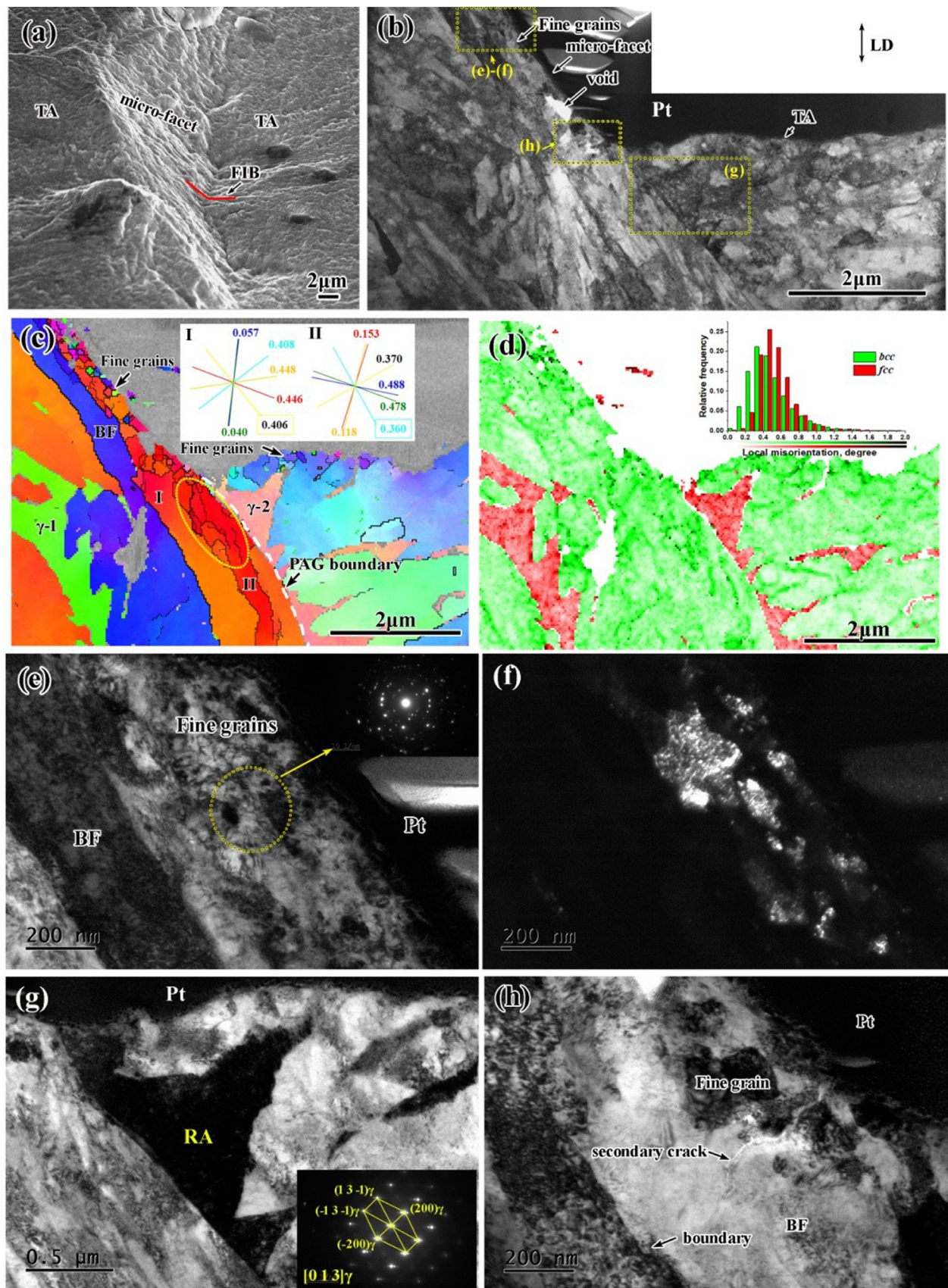


Fig. 9. Microstructural characterization of fatigue crack initiation characteristic area of E-BAT specimen failed at $\sigma_a = 745$ MPa with $N_f = 2.87 \times 10^6$ cycles. (a) SEM image with a tilted angle, the red line shows the position for preparation of FIB sample; (b) TEM image showing the overall microstructure underneath ICA; (c) TKD result showing inverse pole figure and boundary maps, the inset shows slip system trace figure and the numbers are values of maximum Schmid factor of each slip system; (d) TKD results showing local misorientation of bcc and fcc phase; (e) and (f) the bright and dark field TEM images combined with selected area diffraction patterns showing fine grains; (g) TEM image and selected area diffraction patterns of RA; (h) TEM image of secondary crack. LD: loading direction, TA: transition area, BF: bainitic ferrite, RA: retained austenite (For interpretation of the references to color in this figure legend, the reader is referred to the web version of this article.).

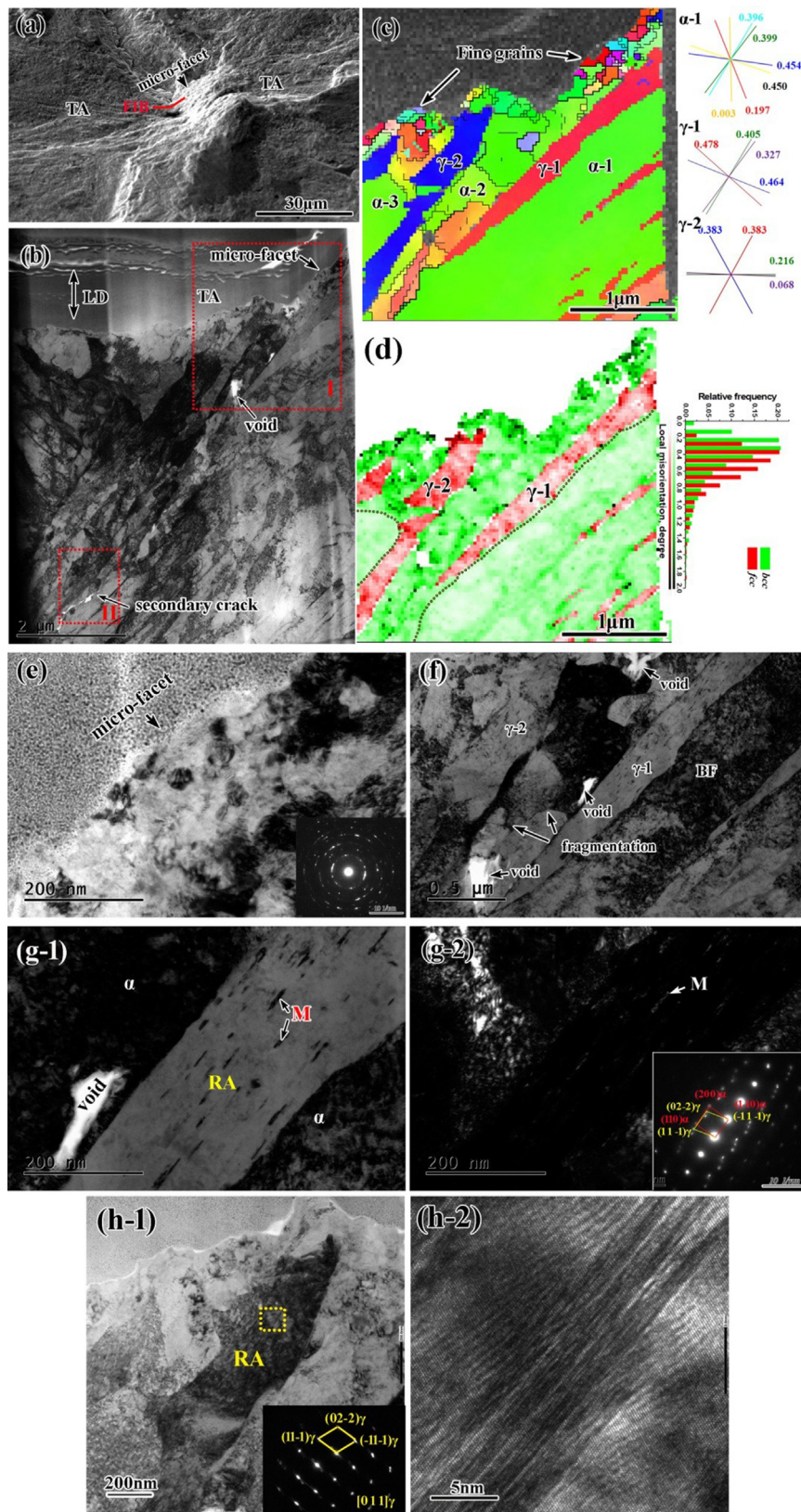


Fig. 10. Microstructural characterization of fatigue crack initiation characteristic area of U-BAT specimen failed at $\sigma_a = 745$ MPa with $N_f = 9.09 \times 10^6$ cycles. (a) SEM image with a tilted angle, the red line showing the location of FIB sample; (b) TEM image showing the overall microstructure underneath ICA; (c) TKD result showing inverse pole figure and boundary maps, the inset shows slip system trace figure and the numbers are values of maximum Schmid factor of each slip system; (d) TKD result showing local misorientation of bcc and fcc phase; (e) the bright-field TEM image combined with selected area diffraction rings showing fine grains; (f) enlarged TEM image showing fragmentation of bainitic ferrite laths; (g-1) bright-field TEM image of of RA and newly formed martensite; (g-2) dark-field TEM image and selected area diffraction patterns showing the newly formed martensite; (h-1) TEM image and selected area diffraction patterns of RA; (h-2) HRTEM image showing the presence of stacking faults. LD: loading direction, TA: transition area, RA: retained austenite, M: martensite (For interpretation of the references to color in this figure legend, the reader is referred to the web version of this article.).

Table 1
Orientation relationship between retained austenite (γ -1, labeled in Fig. 10(c)) and surrounding α phases.

	OR Matrix	Orientation relationship
γ -1 vs. α -1	0.17356 -0.65625 0.734310.98376 0.15023 -0.09826-0.04583 0.73944 0.67167	plane: (1 1 -1) ⁻³ (-3. 0.); 0.8°direc: [1 -1 0] ⁻¹ [1. 1. -1.]; 1.5°
γ -1 vs. α -2	-0.94011 -0.2546 0.226670.34085 -0.71082 0.615270.00447 0.65568 0.75503	plane: (1 -1 -1) ⁻² (-2. 1. -3.); 1.1°direc: [1 0 1] ⁻¹ [1. 1. 1.]; 7.4°
γ -1 vs. α -3	-0.96671 -0.17397 0.187650.25554 -0.69449 0.67260.01331 0.69816 0.71582	plane: (0 1 1) ⁻² (0. 0. 4.); 1.0°direc: [1 1 -1] ⁻¹ [-1. -1. 0.]; 5.0°

Additionally, in comparison to γ -1, the γ -2 grain has a higher average angle of local misorientation, as indicated in Fig. 10(d). But γ -1 grain has a higher Schmid factor compared with the γ -2 grain (Fig. 10(c)). Hence, TEM images and selected area diffraction patterns of γ -1 and γ -2 grains were acquired. From the bright-field TEM image (Fig. 10(g-1)), as well as dark-field TEM image and selected area diffraction patterns (Fig. 10(g-2)), we can see a small fraction of new martensite formed in γ -1. It is found that the newly formed martensite is aligned to the plane of maximum shear stress. Hence, the newly formed martensite might be formed on the slip bands induced by shear stress. The size of newly formed martensite is too small to be detected by TKD. The newly formed martensite can harden the austenite grain of γ -1 and resist local plastic deformation in austenite. Furthermore, the void that forms in α grain near the interface of γ/α can relax some internal stress [42]. In contrast, the γ -2 grain shows the formation of dense stacking faults, as indicated by selected area diffraction patterns and high resolution TEM (HRTEM) image (Fig. 10(h-1) and (h-2)). The planes of stacking fault are found to align along the plane of maximum shear stress. The stacking faults, which are generated because of the dissociation of a perfect dislocation into two partial dislocations, also contributed to plastic deformation [38].

The microstructural characterization near secondary cracks marked by red dashed rectangle II in Fig. 10(b) is presented in Fig. 11. It is found there are several discontinuous voids and secondary cracks formed within a coarse bainitic ferrite lath (thickness of $\sim 0.5 \mu\text{m}$), and distribute along the plane of the maximum shear stress. Hence, the secondary crack can be considered as a stage-I small crack. The longitudinal direction of the BF lath, which is also the direction of distribution of voids and secondary cracks, is aligned to activated $\{110\}_{\alpha}$ slip plane with a high Schmid factor ($SF = 0.412$). However, there is no fine grain near the secondary cracks, as shown in Fig. 11(c). From the local misorientation map in Fig. 11(d), the plastic deformation is concentrated along with the γ/α interface or within the bainitic ferrite lath. There is no obvious strain/stress concentration along the twin boundary of RA.

Fig. 12 illustrates microstructural characterization underneath ICA in another NIIC fracture surface of the U-BAT specimen that failed at $\sigma_a = 680 \text{ MPa}$ with $N_f = 4.88 \times 10^7$ cycles. The TEM sample prepared by FIB covered a part of micro-facet and TA, as shown in Fig. 12(a). It is noted that the micro-facet is aligned to the plane of maximum shear stress. There are fine grains layer and voids along the micro-facet and TA, which can also be confirmed by IPF map in Fig. 12(b) obtained by TKD technology. But the distribution of fine grains layer is discontinuous, e.g., there is no fine grains layer observed near the fracture surface across a bainitic ferrite block (marked as II in Fig. 12(b)). The phenomenon of discontinuous fine grains layer has been previously observed [59]. Interestingly, the fine grains are also formed along the PAG boundary, although this region is not exposed to the fracture surface. The micro-facet is aligned to the longitudinal direction of the bainitic ferrite blocks of both I and II, whose corresponding activated $\{110\}_{\alpha}$ slip planes have nearly the highest Schmid factor ($SF = 0.482$ and 0.467 , respectively). But for the bainitic ferrite block of III, the activated $\{110\}_{\alpha}$ slip plane that is parallel to the fracture surface in TA has a low Schmid factor ($SF = 0.247$). In addition, the activated $\{110\}_{\alpha}$ slip plane of the bainitic ferrite block

of III is not aligned to the longitudinal direction. Hence, the growth path of small cracks depends not only on the magnitude of Schmid factor but also on the spatial distribution of bainitic ferrite block. It seems that the fine grains layer is formed between block II and III (also at the intersection of micro-facet and TA) to facilitate the advancement of a small crack.

The detailed features of fine grains layer and voids in different regions are characterized. Fig. 12(c-1) and (c-2) show the STEM image and selected area diffraction rings of the fine grains layer located along the micro-facet (as marked as region 1 in Fig. 12(a)), respectively. The fine grains have an average size of $\sim 50 \text{ nm}$ and are present around the voids. The voids are formed in the bainitic ferrite lath that is close to RA. The RA partially transformed to martensite. The HRTEM image in Fig. 12(c-3) shows the newly formed martensite. It is also found that the newly formed martensite is aligned to the plane of maximum shear stress, similar to the newly formed martensite in Fig. 10(g-1). In contrast, Fig. 12(d-1) shows the STEM image of the region without fine grains formation (marked by dash rectangle 2 in Fig. 12(a)). The fracture surface (i.e., primary crack path) is aligned to the longitudinal axis of a bainitic ferrite lath. Based on the thickness of bainitic ferrite laths, it seems the micro-crack forms within a coarse bainitic ferrite lath. In addition, the dislocation tangles are limited within the coarse bainitic ferrite lath, as marked by red arrows in Fig. 12(d-1). The inter-lath nanometer-sized film-like RA remains stable, as indicated by the selected area diffraction patterns in Fig. 12(d-2).

Fig. 12(e) shows the fine grains region located between the block II and III of bainitic ferrite (also at the intersection of micro-facet and TA). We can see the formation of voids near the interface of the fine grains region and matrix. Fig. 12(f) is the enlarged TEM image of region 4, as marked in Fig. 12(a). There are dislocation cells and fine grains near the fracture surface. Moreover, the fine grains are formed along the PAG boundary despite far away from the fracture surface. The fine grains along the PAG boundary are shown in Fig. 12(g-1), where the size of fine grains is not uniform. The ultra-fine grain (e.g., marked by d) is formed between the fine grain of b and the PAG boundary. This is a typical phenomenon of continuous dynamic recrystallization (cDRX) [60,61]. The mechanism of cDRX is that the formation of new fine grains is caused by the increase in sub-boundary misorientation brought about by the continuous accumulation of dislocations introduced by the deformation [61]. Unlike static recrystallization and conventional dynamic recrystallization, the cDRX can take place at any temperature [61]. In this study, the continuous accumulation and rearrangement of dislocations take place near the PAG boundary as a result of repeated interaction of slip bands and PAG boundary, which induces the occurrence of local cDRX. In addition, the strain gradient could develop in the vicinity of the PAG boundary and consequently leads to the different sizes of fine grains [61]. The slip bands in α grain adjacent PAG boundary is aligned along the plane of maximum shear stress, as shown in Fig. 12(g-2). This means the formation of slip bands in α grain is driven by the shear stress. In the case of the presence of RA on both sides of PAG boundary, the features of slip bands are shown in Fig. 12(h). It is found that multiple slip bands are activated in the RA grains because of the interaction of dislocation with PAG boundary. The HRTEM image of slip bands in γ -1 grain is shown in Fig. 12(h-2). Furthermore,

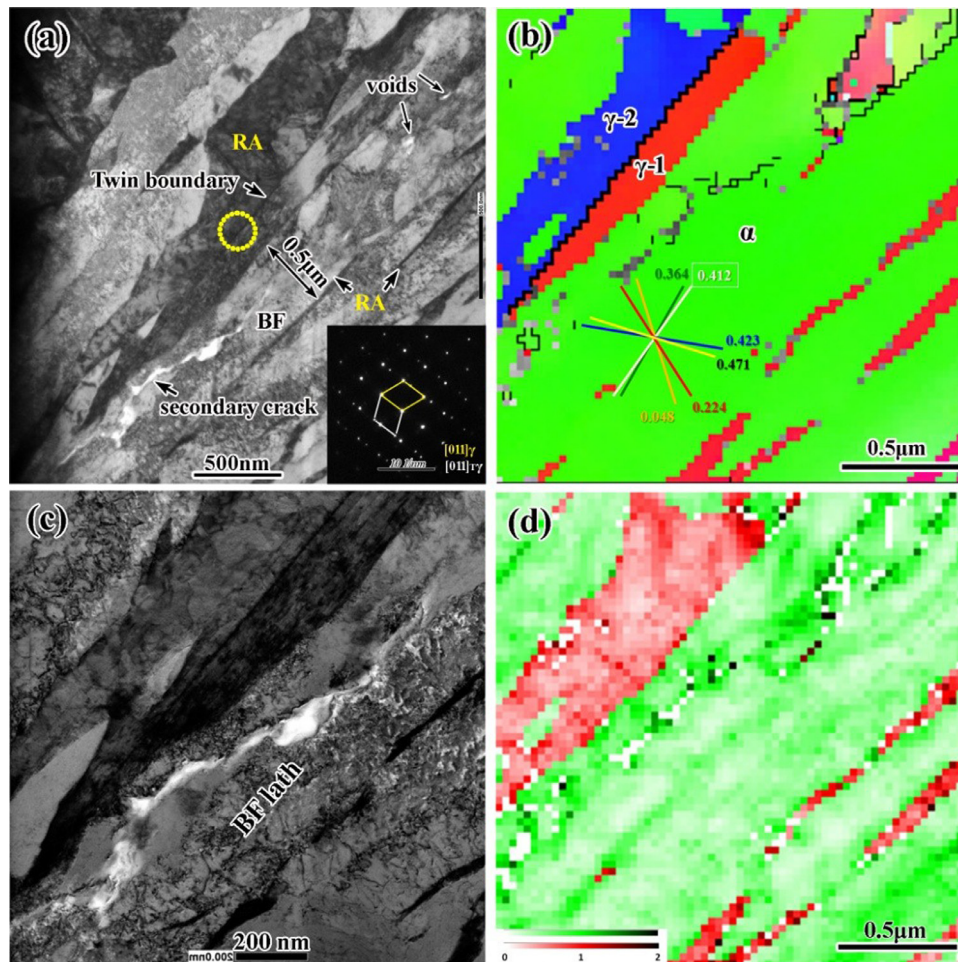


Fig. 11. Microstructural characterization near secondary cracks marked in Fig. 10(b). (a) TEM image with the selected area diffraction patterns of RA twins; (b) TKD result showing inverse pole figure and boundary maps with slip system trace figure; (c) enlarged STEM image; (d) TKD result showing local misorientation of bcc and fcc phase.

the step of PAG boundary is also observed from Fig. 12(h-1). It is suggested that intergranular cracking occurs easily because of high stress concentrations at the step of PAG boundary [62].

4. Discussion

Based on the detailed characterization using different approaches, we conclude that there is a competition between the sub-surface inclusion-induced crack initiation (IICI) and the non-inclusion-induced crack initiation (NIICI) for the studied carbide-free bainitic steels within HCF/VHCF regimes. But the competition mechanisms between the inclusion-induced and non-inclusion-induced crack initiations are still not fully understood. The phenomena may be associated with the size or type of inclusions, the features of microstructure, as well as the interaction between inclusion and microstructure [24,26]. In general, the HCF/VHCF cracks are mostly initiated from the subsurface inclusions in the conventional martensitic high strength steels, but the subsurface NIICI is scarcely observed [11,18]. However, the mechanism of bainitic transformation is different from that of martensitic transformation. The bainitic transformation is a diffusion-controlled transformation but the martensitic is formed by a displacive mechanism [45]. Hence, the distribution of residual stress of bainitic or martensitic microstructure near inclusion could be different [63]. Furthermore, the strength and plasticity of the bainitic microstructure are different from those of the martensitic microstructure due to their different carbon distribution [64]. These could affect the

mode of crack initiation. Besides, there might be some other possible reasons for the competition between IICI and NIICI, which will be studied in the future. In this study, we mainly focus on the micro-mechanism of NIICI of bainitic steel, which could help us to understand the competition mechanism between IICI and NIICI of bainitic steels in the future.

As indicated above, the NIICI is an important and distinct fatigue crack initiation mode of bainitic steels and is associated with the microstructural features and the localized cyclic plastic deformation in microstructure. While from the characterization of the morphology of ICA and local microstructural evolution underneath ICA, it is suggested that there are several micro-mechanisms for the NIICI failure of bainitic steels, as discussed below.

4.1. Transgranular-cracking-assisted NIICI

The first one is the transgranular-cracking-assisted NIICI. Compared with nanometer-sized film-like RA, the micrometer-sized blocky RA and submicron-sized film-like RA generally have a lower strength because of lower carbon content and larger grain size [65]. Under cyclic loading, the critical resolved shear stress is first reached on a slip system with a high Schmid factor in the soft RA grains. Then the slip system is activated, resulting in the generation of slip bands and localized plastic deformation in RA grains. In this case, the neighboring bainitic ferrite laths have to carry additional stresses to maintain the force equilibrium. The superposition of anisotropy stresses with these leads to a situation such

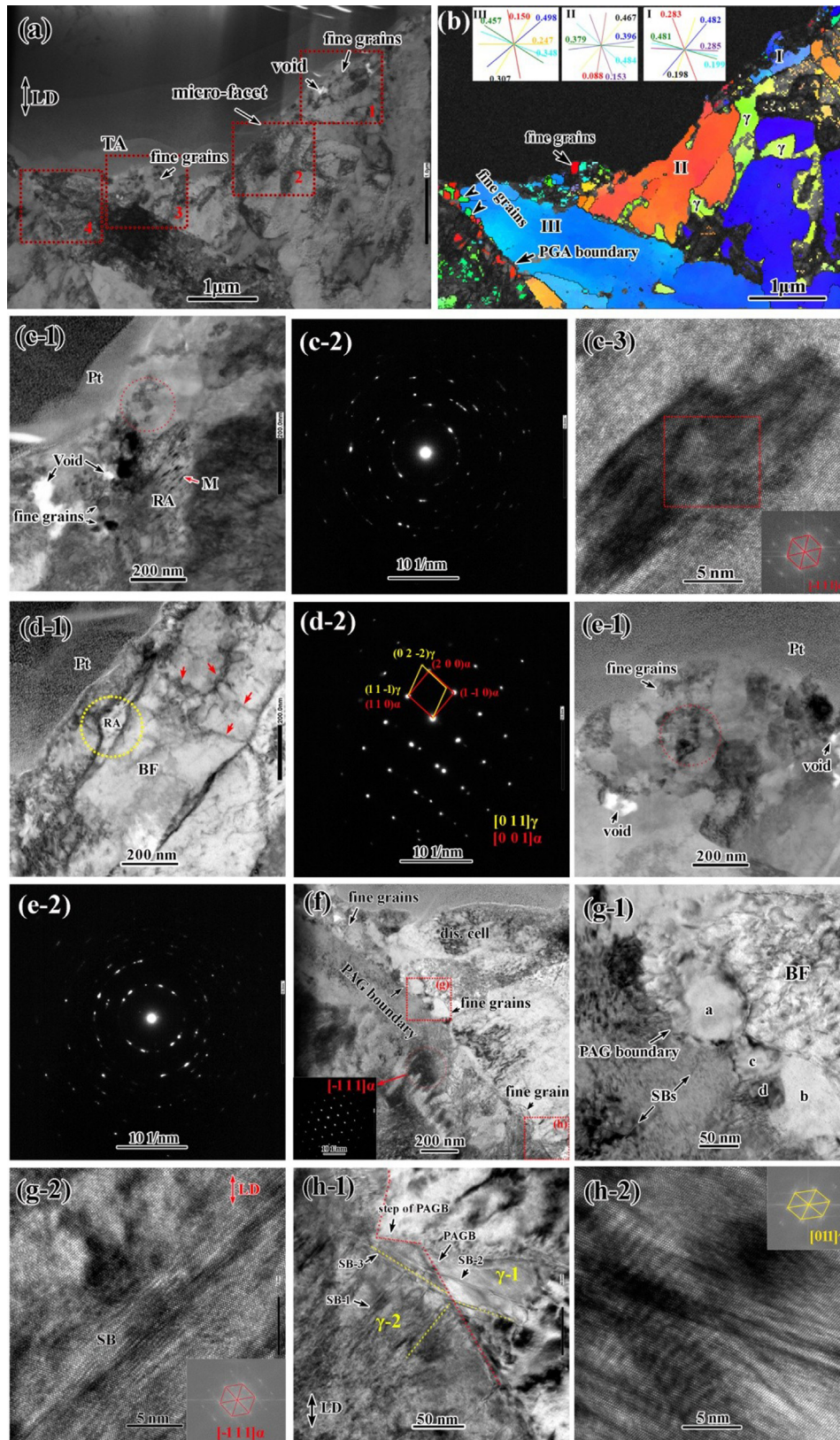


Fig. 12. Microstructural characterization of fatigue crack initiation characteristic area of U-BAT specimen failed at $\sigma_a = 680$ MPa with $N_f = 4.88 \times 10^6$ cycles. (a) TEM image showing the overall microstructures underneath ICA; (b) TKD result showing inverse pole figure and boundary maps, the insets show slip system trace figure and the numbers are value of maximum Schmid factor of each slip system; (c-1): enlarged STEM image showing the fine grains and voids along micro-facet; (c-2): selected area diffraction rings of fine grains; (c-3): HRTEM image showing the newly formed martensite; (d-1) enlarged STEM image showing the region without fine grain along micro-facet; (d-2): selected area diffraction patterns of bainitic ferrite and RA; (e) enlarged STEM image and selected area diffraction rings of fine grains; (f) TEM image showing the fine grains along PAG boundary; (g-1) enlarged TEM image showing the formation of fine grains; (g-2): HRTEM image showing the slip band in bainitic ferrite; (h) enlarged TEM and HRTEM images showing the multiple slip bands in RA grains. LD: loading direction, TA: transition area, RA: retained austenite, BF: bainitic ferrite, M: martensite.

that the critical stress in the neighboring bainitic ferrite laths is reached, resulting in localized plastic deformation in bainitic ferrite laths [38]. The cyclic softening and hardening of RA affect the stress/strain partitioning between RA and bainitic ferrite laths and consequently the accumulation of plastic deformation in bainitic ferrite laths [42]. As indicated in Fig. 10(g) and (h), the RA transformed to martensite (γ -1 grain) or generated stacking faults (γ -2 grain). The newly formed martensite laths and stacking faults are arranged along the maximum shear stress plane, which are driven by the localized shear strain. Consequently, the plastic deformation takes place in the bainitic ferrite laths between the two RA grains (γ -1 and γ -2), resulting in the fragmentation of bainitic ferrite (Fig. 10(f)). The ferrite phase endures less plastic deformation before crack initiation compared to the more ductile austenite phase. Hence, the localized shear strain in austenite does not directly lead to crack initiation; instead, first there is the formation of micro-crack in the ferrite phase [38]. This is confirmed in Fig. 10(f) that shows that the void is formed in the bainitic ferrite lath near RA. With the increase in number of cycles, the plastic deformation continues to be accumulated in bainitic ferrite lath, resulting in the fragmentation of bainitic ferrite lath and finally the formation of new fine grains. As indicated in Fig. 12(c), the fine grains are formed surrounding the voids. It is suggested that the formation of fine grains reduces the local threshold ($\Delta K_{th, local}$) for crack propagation and promotes the coalescence of voids [16]. We can see that the scenario of transgranular-cracking-assisted NIICI is associated with the generation of slip bands in the soft RA resulting in the plastic deformation of neighboring bainitic ferrite laths.

Besides this scenario, there is another scenario of transgranular-cracking-assisted NIICI when the generation of slip bands takes place first in the coarse bainitic ferrite lath. The strength of the bainitic ferrite lath decreases with the increase of lath thickness [65]. Furthermore, the inter-lath film-like RA with nanometer-size does not easily experience plastic deformation. In this situation, the dislocations on a slip system with high a Schmid factor in coarse bainitic ferrite lath would glide first, driven by the maximum shear stress. When that slip plane is parallel to the longitudinal axis of the bainitic ferrite lath, it is aligned to the plane of maximum shear stress, and the dislocations glide easily resulting in the generation of slip bands within the bainitic ferrite lath. Based on the persistent slip band structure model proposed by Tanaka and Mura [66], the plastic deformation is localized into a small volume within slip bands. With the increase in the number of cycles, the dislocation density within slip bands increases resulting in the formation of dislocation walls in slip bands. Subsequently, the micro-crack is nucleated from dislocation walls in slip bands because of the collapse of walls, as described by Zhai et al. [67]. The mode of crack initiation is referred to as “shear cracking mode” or “damage accumulation mode”, where the crack nucleation and coalescence are controlled by cyclic shear stress [68]. As shown in Fig. 11, the small cracks are formed along with the $\{110\}_\alpha$ slip plane with nearly highest Schmid factor in bainitic ferrite lath and propagated along the longitudinal axis of the lath. In addition, the plastic deformation is mainly limited within slip bands and is very small outside of the slip bands [49,68]. In this case, the fine grains will not form along the micro-cracks, as indicated in Figs. 11, 12(b) and 12(d). Schematic illustrations of the two scenarios of transgranular-cracking-assisted NIICI are presented in Fig. 13(a) and (b), respectively. It is found that the different deformation/fracture behaviors of the bainitic ferrite laths are mainly caused by the different sizes of bainitic ferrite lath and inter-lath RA. The local strength generally decreases with the increase of the sizes of bainitic ferrite and RA [65], which determines the sequence of local plastic deformation of each phase and the consequent stress/strain partitioning.

4.2. Intergranular-cracking-assisted NIICI

The second one is the intergranular-cracking-assisted NIICI. Here, the intergranular-cracking means the crack initiation along the PAG boundaries. As discussed above, the slip bands are generated along with a system with a high Schmid factor in preferentially oriented grains (e.g., either soft RA or coarse bainitic ferrite lath). As indicated in Fig. 12(g-2) and (h-2), the slip bands in both α and γ phases are observed. The slip bands impinge into the PAG boundaries if there are not any strong barriers to dislocation glide. The consequences of the interaction between slip bands and PAG boundaries depend on the microstructural characteristics of adjacent PAG. If there are blocky M/A islands located at the PAG boundaries, the intergranular crack initiation occurs through cleavage cracking because of the brittle characteristic of high-carbon martensite, as shown in Fig. 7(b). This has been discussed in our recent study [29,43].

In another case when there is a ductile phase (such as bainitic ferrite) located at the PAG boundaries, more cycles are required to accumulate more plastic deformation before crack initiation. The fine grains may be formed through local continuous dynamic recrystallization (cDRX) as a result of the repeated interaction of slip bands and PAG boundaries on a localized volume, as indicated in Fig. 12(f) and (g). However, recent work on the fatigue performance of the additive manufacturing (AM) 304L austenitic stainless steels reveals that the local recrystallization behavior has a detrimental effect on crack initiation, because of a strong strain mismatch between the coarse grains and fine grains [69]. In addition, the step of PAG boundary is also formed on the impingement of slip bands (Fig. 12(h-1)). Once the intergranular crack initiation takes place because of the stress concentration at the step of PAG boundary [62], the fine grains facilitate the advancement of small cracks because of the decrease of local threshold value ($\Delta K_{th, local}$) of fine grains region [16]. In this case, the fine grains layer is observed at least on one side of the fracture surface along PAG boundaries. Schematic illustrations of the two scenarios of intergranular-cracking-assisted NIICI are shown in Fig. 13(c) and (d), respectively.

It may be noted that the NIICI failure is attributed to the combination of the above mechanisms rather than a single one. For instance in Fig. 8, a part of the micro-facet is occupied by M/A showing cleavage facet, whereas the other part exhibited fragmented microstructure (i.e., grain refinement). Furthermore, we can see in Fig. 12(a) and (b) the discontinuous distribution of fine grains layers along the micro-facet. The different features of fracture surface correspond to the various scenarios of mechanisms taking place in NIICI event. It is suggested that the combination of these scenarios and the order in which these scenarios are triggered depend on the microstructures and the development of localized plastic deformation, as indicated in Fig. 13.

Meanwhile, we can also see that the fine grains layer is formed under some scenarios of mechanisms rather than all scenarios, as indicated in Fig. 13. The formation of fine grains is attributed to the fragmentation of bainitic ferrite lath caused by localized plastic deformation. In our study, there is the repeated interaction between PAG boundaries and slip bands leading to the formation of fine grains through local continuous dynamic recrystallization. The bainitic ferrite in bainite exhibits a hierarchical structure with packet, block and lath. The boundaries of bainitic ferrite packet and block are high-angle grain boundaries [46]. Hence, it is implied that the interaction of slip bands and the block/packet boundaries also promotes the formation of fine grains. For instance, the fine grains are formed at the boundary between two blocks of bainitic ferrite, as indicated in Fig. 12(b). Furthermore, the formation of fine grains is also found in TA area, which promotes the transition of small cracks into long cracks due to decrease of $\Delta K_{th, local}$.

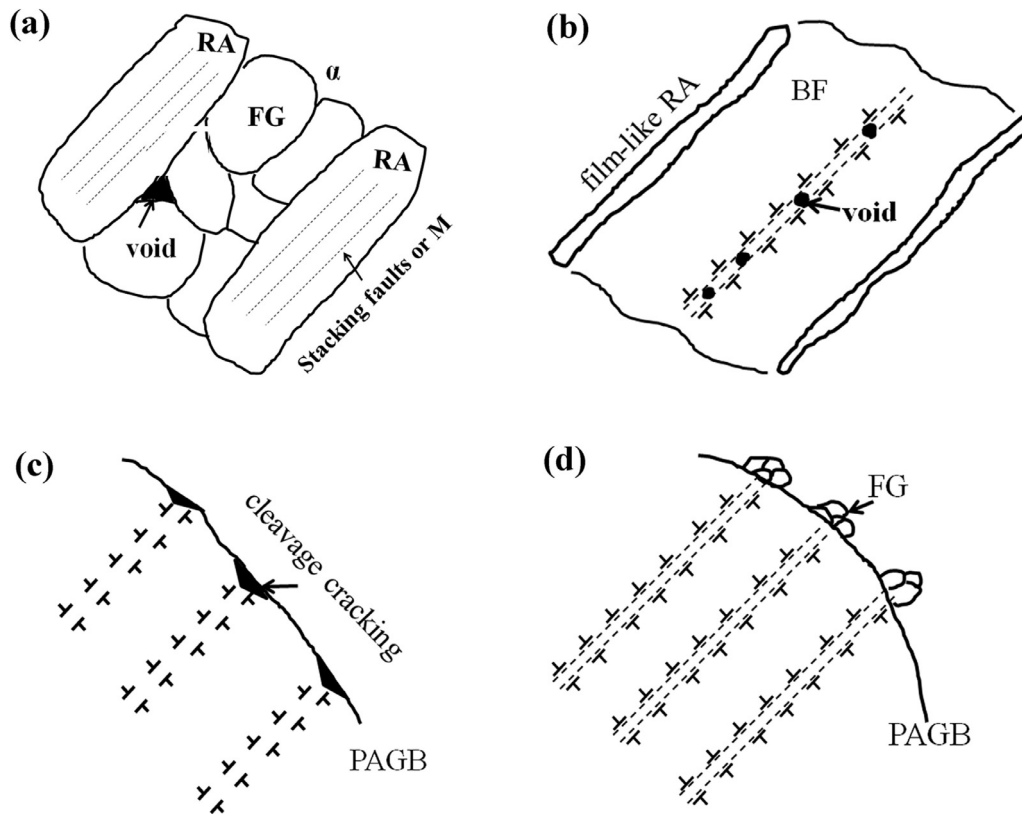


Fig. 13. Schematic illustration of scenarios of mechanisms of NIICI failure. (a) Transgranular-cracking-assisted NIICI with fine grains formation; (b) transgranular-cracking-assisted NIICI without fine grain formation; (c) intergranular-cracking-assisted NIICI without fine grain formation; and (d) intergranular-cracking-assisted NIICI with fine grains formation. RA: retained austenite, BF: bainitic ferrite, PAGB: prior austenite grain boundary, FG: fine grain.

Based on the mechanisms of NIICI failure, the RA has a determining effect on triggering of different scenarios, which is associated with the size, distribution and stability of RA, as indicated in Fig. 13(a) and (b). It was observed that the sub-micron-sized RA grains partially transform to martensite with a small size or generate stacking faults and twins under cyclic loading. The newly transformed products of RA are generally aligned to the plane of maximum shear stress. Hence, the newly formed interfaces (such as the interface of RA and newly formed martensite with small size, twinning boundary) do not become crack nucleation sites, as indicated in Fig. 11(d). Meanwhile, the transformation of RA absorbs some energy and the transformation products of RA could harden the RA [70], which affects the development of localized plastic deformation and consequently crack initiation event. On the other hand, our recent works revealed that the inter-lath film-like RA at the straight front of small crack tip transformed to martensite, which arrested the growth of small crack and led to the change in the active slip systems [30]. In this study, we can see that the nanometer-sized inter-lath RA films that are close to the plane of maximum shear stress remained stable, such that the dislocation glide is limited within in bainitic ferrite lath, as shown in Fig. 12(d-1).

5. Conclusion

We studied the HCF/VHCF behaviors of advanced carbide-free bainitic (CFB) steels with two different levels of the size of inclusion. The multiphase microstructure obtained by bainitic austempering (BAT) treatment is composed of bainitic ferrite, retained austenite with different morphologies and martensite/austenite constituent. There is a competitive effect of microstructure and inclusion on the process of fatigue crack initiation during HCF/VHCF

failure. The subsurface microstructural fatigue crack initiation, referred to as “non-inclusion induced crack initiation, NIICI”, is a leading failure mode for the CFB steels within HCF/VHCF regimes. The mechanisms of NIICI failure were discussed based on the detailed characterization of the fracture surface and the local microstructural evolution. The main conclusions are as follows:

- (1) The crack initiation characteristic area (ICA) of NIICI fracture surface is composed of a micro-facet that is close to the plane of maximum shear stress and a surrounding undulated transition area (TA). The average values of stress intensity factor (SIF) range at the periphery of ICA is close to the threshold SIF for the propagation of long crack. There are discontinuous fine grains and micro-voids formed near the surface of micro-facet and TA.
- (2) There are multiple micro-mechanisms responsible for the NIICI failure of bainitic steels, including two scenarios of transgranular-cracking-assisted NIICI and two scenarios of intergranular-cracking-assisted NIICI. The combination of these scenarios and the order in which these scenarios are triggered depend on the microstructures and the development of localized plastic deformation.
- (3) The fine grains layer is formed under some scenarios of failure mechanisms rather than all the scenarios. The fine grains are formed through the fragmentation of bainitic ferrite lath caused by localized plastic deformation or via the local continuous dynamic recrystallization because of repeated interaction between slip bands and prior austenite grain boundaries. The formation of fine grains facilitated the advancement of small cracks.
- (4) The retained austenite (RA) has a determining effect on triggering different scenarios of mechanisms of NIICI failure, which

is associated with the morphology, distribution and stability of RA.

Acknowledgments

The authors (at BJT and TU) gratefully acknowledge the funding by National Key Technologies Research and Development Program of China (2017YFB0304500). G. Gao and B. Bai acknowledge the support from National Natural Science Foundation of China (No. 51771014) and Joint Funds of National Natural Science Foundation of China (No. U1834202). The authors are extremely grateful to Professor R.D.K. Misra for his willingness to collaborate.

Data Availability

Data will be made available on request

Declarations of Competing Interest

None

Supplementary materials

Supplementary material associated with this article can be found, in the online version, at [doi:10.1016/j.jmst.2021.08.060](https://doi.org/10.1016/j.jmst.2021.08.060).

References

- Z. Dai, H. Chen, R. Ding, Q. Lu, C. Zhang, Z. Yang, S. van der Zwaag, *Mater. Sci. Eng. R* 143 (2021) 100590.
- F.G. Caballero, H. Bhadeshia, K.J.A. Mawella, D.G. Jones, P. Brown, *Mater. Sci. Tech.* 17 (2001) 512–516 Lond..
- X. Long, F. Zhang, Z. Yang, B. Lv, *Mater. Sci. Eng. A* 715 (2018) 10–16.
- Z. Yang, F. Zhang, *ISIJ Int.* 60 (2020) 18–30.
- X. Gui, K. Wang, G. Gao, R.D.K. Misra, Z. Tan, B. Bai, *Mater. Sci. Eng. A* 657 (2016) 82–85.
- C. Klinger, D. Bettge, *Eng. Fail. Anal.* 35 (2013) 66–81.
- S. Fintová, P. Pokorný, P. Fajkoš, P. Hutař, *Eng. Fail. Anal.* 115 (2020) 104668.
- B. Pyttel, D. Schwerdt, C. Berger, *Int. J. Fatigue* 33 (2011) 49–58.
- W. Li, R. Sun, N. Gao, P. Wang, T. Sakai, *Fatigue Fract. Eng. Mater. Struct.* 42 (2019) 2383–2396.
- D. Jeddí, T. Palin-Luc, *Fatigue Fract. Eng. Mater. Struct.* 41 (2018) 969–990.
- S.X. Li, *Int. Mater. Rev.* 57 (2012) 92–114.
- Y. Murakami, T. Nomoto, T. Ueda, Y. Murakami, *Fatigue Fract. Eng. Mater. Struct.* 23 (2000) 893–902.
- K. Shiozawa, Y. Morii, S. Nishino, L. Lu, *Int. J. Fatigue* 28 (2006) 1521–1532.
- T. Sakai, N. Oguma, A. Morikawa, *Fatigue Fract. Eng. Mater. Struct.* 38 (2015) 1305–1314.
- Y. Hong, Z. Lei, C. Sun, A. Zhao, *Int. J. Fatigue* 58 (2014) 144–151.
- P. Grad, B. Reuschler, A. Brodyanski, M. Kopnarski, E. Kerscher, *Scr. Mater.* 67 (2012) 838–841.
- Y. Hong, X. Liu, Z. Lei, C. Sun, *Int. J. Fatigue* 89 (2016) 108–118.
- G. Chai, T. Forsman, F. Gustavsson, C. Wang, *Fatigue Fract. Eng. Mater. Struct.* 38 (2015) 1315–1323.
- D. Spriestersbach, E. Kerscher, *Int. J. Fatigue* 111 (2018) 93–100.
- M. Zhu, L. Jin, F. Xuan, *Acta Mater.* 157 (2018) 259–275.
- J.P. Sippel, E. Kerscher, *Appl. Sci.* 10 (2020) 8475.
- K.S. Chan, *Int. J. Fatigue* 32 (2010) 1428–1447.
- G. Chai, N. Zhou, S. Ciurea, M. Andersson, R.L. Peng, *Scr. Mater.* 66 (2012) 769–772.
- P. Zhao, G. Gao, R.D.K. Misra, B. Bai, *Mater. Sci. Eng. A* 630 (2015) 1–7.
- G. Gao, B. Zhang, C. Cheng, P. Zhao, H. Zhang, B. Bai, *Int. J. Fatigue* 92 (2016) 203–210.
- G. Gao, Q. Xu, H. Guo, X. Gui, B. Zhang, B. Bai, *Mater. Sci. Eng. A* 739 (2019) 404–414.
- X. Pan, Y. Hong, *Fatigue Fract. Eng. Mater. Struct.* 42 (2019) 1950–1964.
- Y. Wu, J.R. Liu, H. Wang, S.X. Guan, R. Yang, H.F. Xiang, *J. Mater. Sci. Technol.* 34 (2018) 1189–1195.
- W. Li, R. Sun, P. Wang, X. Li, Y. Zhang, T. Hu, C. Li, T. Sakai, *Scr. Mater.* 194 (2021) 113613.
- G. Gao, R. Liu, K. Wang, X. Gui, R.D.K. Misra, B. Bai, *Scr. Mater.* 184 (2020) 12–18.
- P. Chowdhury, H. Sehitoglu, *Fatigue Fract. Eng. Mater. Struct.* 39 (2016) 652–674.
- G. Chai, *Int. J. Fatigue* 28 (2006) 1533–1539.
- H. Abdesselam, J. Crepin, A. Pineau, A.L. Rouffie, P. Gaborit, L. Menut-Tournadre, T.F. Morgeneyer, *Int. J. Fatigue* 106 (2018) 132–142.
- F.C. Zhang, X.Y. Long, J. Kang, D. Cao, B. Lv, *Mater. Des.* 94 (2016) 1–8.
- R. Rementeria, L. Morales-Rivas, M. Kuntz, C. Garcia-Mateo, E. Kerscher, T. Sourmail, F.G. Caballero, *Mater. Sci. Eng. A* 630 (2015) 71–77.
- A. Kumar, A. Singh, *Mater. Sci. Eng. A* 743 (2019) 464–471.
- M.C. Marinelli, M. Balbi, U. Krupp, *Int. J. Fatigue* 143 (2021) 106014.
- B. Dönges, A. Gierler, U. Krupp, C.P. Fritzen, H.J. Christ, *Mater. Sci. Eng. A* 589 (2014) 146–152.
- G. Chai, *Int. J. Fatigue* 28 (2006) 1611–1617.
- C.Y. Huo, H.L. Gao, *Mater. Charact.* 55 (2005) 12–18.
- M. Koyama, Z. Zhang, M. Wang, D. Ponge, D. Raabe, K. Tsuzaki, H. Noguchi, C.C. Tasan, *Science* 355 (2017) 1055–1057.
- H. Fu, B. Dönges, U. Krupp, U. Pietsch, C.P. Fritzen, X. Yun, H.J. Christ, *Acta Mater.* 199 (2020) 278–287.
- G. Gao, K. Wang, H. Su, X. Gui, Z. Li, R.D.K. Misra, B. Bai, *Int. J. Fatigue* 139 (2020) 105804.
- G. Gao, H. Zhang, X. Gui, P. Luo, Z. Tan, B. Bai, *Acta Mater.* 76 (2014) 425–433.
- Z.G. Yang, H.S. Fang, *Curr. Opin. Solid State Mater.* 9 (2005) 277–286.
- T. Furuhashi, H. Kawata, S. Morito, T. Maki, *Mater. Sci. Eng. A* 431 (2006) 228–236.
- F. Bachmann, R. Hielscher, H. Schaeben, *Solid State Phenom.* 160 (2010) 63–68.
- S. Morito, X. Huang, T. Furuhashi, T. Maki, N. Hansen, *Acta Mater.* 54 (2006) 5323–5331.
- M.D. Sangid, *Int. J. Fatigue* 57 (2013) 58–72.
- U. Krupp, H. Knobbe, H.J. Christ, P. Köster, C.P. Fritzen, *Int. J. Fatigue* 32 (2010) 914–920.
- Y. Murakami, *Eng. Fract. Mech.* 22 (1985) 101–114.
- Z. Lei, Y. Hong, J. Xie, C. Sun, A. Zhao, *Mater. Sci. Eng. A* 558 (2012) 234–241.
- Y. Murakami, *Metal Fatigue: Effects of Small Defects and Nonmetallic Inclusions*, Elsevier, 2002.
- Y. Murakami, M. Endo, *Int. J. Fatigue* 16 (1994) 163–182.
- M.J. Santofimia, L. Zhao, R. Petrov, C. Kwakernaak, W.G. Sloof, J. Sietsma, *Acta Mater.* 59 (2011) 6059–6068.
- M.C. Marinelli, I. Alvarez-Armas, U. Krupp, *Mater. Sci. Eng. A* 684 (2017) 254–260.
- X.F. Gu, T. Furuhashi, W.Z. Zhang, *J. Appl. Cryst.* 49 (2016) 1099–1106.
- M. Kamaya, *Mater. Charact.* 60 (2009) 1454–1462.
- Q. Song, C. Sun, *Mater. Sci. Eng. A* 771 (2020) 138648.
- A. Galiyev, R. Kaibyshev, G. Gottstein, *Acta Mater.* 49 (2001) 1199–1207.
- T. Sakai, A. Belyakov, R. Kaibyshev, H. Miura, J.J. Jonas, *Prog. Mater. Sci.* 60 (2014) 130–207.
- M.D. Sangid, H.J. Maier, H. Sehitoglu, *Acta Mater.* 59 (2011) 328–341.
- P.J. Withers, H.K.D.H. Bhadeshia, *Mater. Sci. Tech.* 17 (2001) 366–375 Lond..
- D. Foster, M. Paladugu, J. Hughes, M. Kapousidou, C. Barcellini, D. Daisenberger, E. Jimenez-Melero, *Materialia* 14 (2020) 100948.
- G. Gao, B. Gao, X. Gui, J. Hu, J. He, Z. Tan, B. Bai, *Mater. Sci. Eng. A* 753 (2019) 1–10.
- K. Tanaka, T. Mura, *J. Appl. Mech.* 48 (1981) 97–103.
- T. Zhai, J.W. Martin, G.A.D. Briggs, *Acta Metall.* 43 (1995) 3813–3825.
- S. Hamada, K. Zhang, M. Koyama, M. Ueda, H. Noguchi, *Int. J. Fract.* 222 (2020) 111–122.
- H. Zhang, M. Xu, Z. Liu, C. Li, Y. Zhang, *Mater. Charact.* 177 (2021) 111159.
- M. Soleimani, A. Kalhor, H. Mirzadeh, *Mater. Sci. Eng. A* 795 (2020) 140023.